Electrical control of antiferromagnetic domain walls in Weyl semimetals

Yuriy G. Semenov[1,2] and Ki Wook Kim[1,*]

[1]*Department of Electrical and Computer Engineering, North Carolina State University, Raleigh, North Carolina 27695, USA*
[2]*V. Lashkaryov Institute of Semiconductor Physics, National Academy of Sciences of Ukraine, Kyiv 03680, Ukraine*

(Received 8 July 2022; accepted 21 March 2023; published 29 March 2023)

The electric-field-induced angular force on the Néel vector in antiferromagnetic (AFM) Weyl semimetals (WSMs) is theoretically investigated. Unlike in the ferromagnetic (FM) counterparts, the magnetic textures in the AFM WSMs, such as the domain walls (DWs) appear to lack the torsion in the magnetization and, thus, unable to benefit from this highly efficient mechanism that originates from the axial magnetic effect. Contrarily, our calculations illustrate that the addition of the Dzyaloshinskii-Morya interaction can introduce a twist in the magnetization around the DW location, giving rise to a nonzero axial magnetic field. This axial magnetic field, when combined with an external electric field, can lead to an imbalance in the fermion density of Weyl cones of opposite chirality and, thus, a spatially localized net electron spin polarization. The resulting effective exchange field can exert an angular force on the AFM textures for spatial movement, which can be significant in certain AFM WSMs even under a moderate external electric field. The dynamics of the DW motion under this emergent angular force is analyzed by considering the balance of energy absorption and dissipation. Our investigation reveals the need to account for the contribution of the exchange dissipation mechanism beyond the typical Gilbert-like (relativistic) term to compensate the unusual superlinear rate of energy absorption by the AFM textures. The obtained DW velocity vs electric-field characteristics show a significant speedup for the Néel DWs in the AFM WSMs over the counterparts in the FM WSMs as well as those in the nontopological magnets. The analysis also elucidates the dependence of the DW motion on the DW chirality in these materials. Our results clearly indicate the significance of the energy-efficient axial magnetic effect in the dynamics of spin textures in AFM WSMs with broken inversion symmetry.

DOI: 10.1103/PhysRevB.107.094434

I. INTRODUCTION

In the incipient field of spintronics, device-enabling physical processes that utilize the exceptional properties of antiferromagnets (AFMs), such as fast switching dynamics and suppressed stray magnetic fields have become a major point of interest as documented in the recent reviews [1–7]. The long-standing challenges in the electrical detection of the state of the AFM order parameter can now be resolved with the aid of anisotropic magnetoresistance and spin-Hall effect (see, for instance, Refs. [3,6]). The approaches based on a spin-polarized electrical current (such as the spin-transfer, spin-orbit, and Néel spin–orbit torques) have successfully demonstrated the control of magnetic dynamics in collinear AFMs where a large driving current density (10^7–10^8 A/cm^2) is invariably required [8–10] as in the comparable ferromagnetic (FM) systems. Other, potentially more energy efficient mechanisms to induce an effective torque have also been explored for currentless Néel vector switching in nanoparticles [11]. In the case of AFM textures, such as a domain wall (DW), electrical manipulation becomes more challenging, particularly, for currentless processes as a sufficiently strong spin torque must be applied over the entire trace of DW propagation [12–14]. Even for those mediated by the spin-polarized (thus, spin) current, the necessary high electrical current density employed over a substantial duration causes unwanted Joule heating.

An alternative, potentially more-energy-efficient approach for the electrical control of magnetic textures was proposed recently by exploiting the unique properties of Weyl semimetals (WSMs) [15–17]. These materials possess a relativisticlike linear dispersion for three-dimensional electrons, resembling Weyl fermions, when the Fermi energy is located close to the valley-related Weyl nodes. The topological protection of WSMs is characterized by the broken inversion, or time reversal, or both symmetries ($\mathcal{P}$ and $\mathcal{T}$, respectively); thus, Weyl fermions can coexist with magnetically ordered crystals. A crucial advantage of such a topologically nontrivial magnetic WSM (particularly, a FM WSM) is the emergent exchange field of Weyl fermions and the subsequent torque induced by the axial anomaly [15]. More specifically, an imbalance in the carrier chirality caused by the anomaly (i.e., an axial current $\mathbf{j}^5$) leads to net spin polarization due to the strong spin-orbit coupling, whereas the curl of the magnetization plays the role of an axial magnetic-field $\mathbf{B}_5$. The resulting torque is determined by $\mathbf{B}_5$ and the applied electric-field $\mathbf{E}$ (rather than the spin-polarized current in the conventional spin torque mechanisms). The location of nonzero $\mathbf{B}_5$ is associated with that of magnetic textures (such as, a DW) where absorption of the electric energy (i.e., energy loss) is expected to be much smaller than the corresponding operation in a

*kwk@ncsu.edu

conventional magnet. Even when the textures are driven by an external magnetic field instead, FM WSMs are expected to offer similar advantages [17].

The prospect of correspondingly efficient electrical control of magnetic textures provides a strong motivation to examine the axial magnetic effects in AFM WSMs. However, a cursory analysis suggests that they may not benefit from this effect due to the absence of net magnetization (thus, $\mathbf{B}_5 = 0$). More fundamentally, the ground state of bipartite collinear AFM WSMs possesses the combined $\mathcal{TP}$ symmetry, hence, retaining the double degeneracy of the band structure that is incompatible with Weyl fermions [18–20]. As such, the remedy may be to utilize the weakly FM structures of low crystalline symmetry. It is well known that the AFM sublattices when combined with strong spin-orbit coupling, can undergo canting through the Dzyaloshinskii-Moriya interaction (DMI) in the crystals with broken $\mathcal{P}$ symmetry. The resulting appearance of a small but finite net magnetization makes them akin to weak FMs. Moreover, temporal evolution of an AFM texture unavoidably induces a finite magnetic moment, which also breaks the $\mathcal{TP}$ symmetry and restores the electronic band structure of Weyl fermions.

Building on these observations, we theoretically investigate the effect of an external electric field on the Néel vector dynamics in low-symmetry AFM WSMs. Our analysis clearly illustrates that the axial current and net electron-spin polarization can indeed appear in an AFM texture subject to the DMI. The resulting angular force on the Néel vector (associated with the corresponding spin torque on each sublattice) enables efficient electrical control of its dynamics. Further investigation reveals the characteristics of transient AFM DW motion by considering the balance of energy absorption and dissipation in the magnetic texture. The distinctive features of electrically controlled DW dynamics in the AFM WSMs are highlighted in comparison with those in the FM counterparts.

II. THEORETICAL MODEL

A. General approach

Since the focus is to examine the distinctive qualitative characteristics of the magnetic texture dynamics, the details of the electronic band structure and its topological properties in AFM WSMs (which can be readily found in the literature [19–22]) are not critical in the present analysis except the presence of multiple Weyl node pairs associated with the broken inversion symmetry. Accordingly, we start with a minimal Hamiltonian describing an electron with momentum $\mathbf{k}$ and spin $\mathbf{s}$ in the vicinity of a Weyl point at $\mathbf{K}_n$ that is, interacting with spin moments $\mathbf{S}_j$ localized at lattice sites $j = j_A$ for sublattice A and $j = j_B$ for sublattice B of the AFM texture,

$$H_n = \eta_n \hbar v_F (\mathbf{k} - \mathbf{K}_n) \cdot \mathbf{s} - \sum_{j_A} \alpha_{j_A} \mathbf{S}_{j_A} \cdot \mathbf{s} - \sum_{j_B} \alpha_{j_B} \mathbf{S}_{j_B} \cdot \mathbf{s}. \tag{1}$$

Here, η_n ($= \pm 1$) denotes the chirality of the Weyl cone n and v_F denotes the Fermi velocity of the electron. For simplicity, we consider the type-I WSM ignoring the possible tilt of the cone in the first term of Eq. (1). The strength of the carrier-ion exchange interaction in the second and third terms is described by the exchange integrals $\alpha_{j_{A(B)}}$, which are proportional to the electron density at the lattice sites $j_{A(B)}$.

In the case when the carrier density does not show an appreciable spatial variation at each sublattice site (i.e., $\alpha_{j_A} = \alpha_{j_B}$) and the dimensions of the AFM textures (e.g., the DW width) are sufficiently larger than the lattice constant, the macroscopic spin moments $\sum \mathbf{S}_{j_{A(B)}}$ ($\sim \mathbf{M}_{A(B)}$) can be represented by the continuous sublattice magnetizations $\mathbf{M}_{A(B)} = \mathbf{M}_{A(B)}(\mathbf{r})$. Since both the structure local magnetization $\mathbf{M}(\mathbf{r})$ and the Néel vector $\mathbf{L}(\mathbf{r})$ can then be expressed as $\mathbf{M}_A(\mathbf{r}) + \mathbf{M}_B(\mathbf{r}) = 2M_s\mathbf{m}(\mathbf{r})$ and $\mathbf{M}_A(\mathbf{r}) - \mathbf{M}_B(\mathbf{r}) = 2M_s\mathbf{n}(\mathbf{r})$, respectively, with the sublattice magnetization M_s, the Hamiltonian in Eq. (1) may be reduced to a more conventional form for node n as

$$H_n = \eta_n \hbar v_F (\mathbf{k} - \mathbf{K}_n) \cdot \mathbf{s} - J\mathbf{m} \cdot \mathbf{s}, \tag{2}$$

where constant J signifies the strength of the exchange interaction.

Applying this model to a magnetic texture dynamics takes an additional dependence of $\mathbf{m}(\mathbf{r})$ and $\mathbf{n}(\mathbf{r})$ on time t; i.e., $\mathbf{m}(\mathbf{r}, t)$ and $\mathbf{n}(\mathbf{r}, t)$. As in the FM WSMs, the key feature of the Hamiltonian given in Eq. (2) elicits the formal analogy of the term $\mathbf{A}_5 = J\mathbf{m}/q_e$ with the vector potential in the classical electrodynamics provided the Fermi velocity v_F mimics the light velocity, and q_e is the unit electron charge [15,23]. Such a vector potential would subject the electrons to an axial electric-field $\mathbf{E}_5 = -\frac{1}{v_F}\partial_t \mathbf{A}_5 = -\frac{J}{v_F q_e}\partial_t \mathbf{m}$ and an axial magnetic-field $\mathbf{B}_5 = \nabla \times \mathbf{A}_5 = \frac{J}{q_e}\nabla \times \mathbf{m}$, whose signs depend on the chirality η_n of the Weyl cone n. Thus, it is not surprising that the anomalous Hall current $\mathbf{j}_n (\sim \mathbf{B}_5 \times \mathbf{E})$ induced in the presence of an external electric-field $\mathbf{E}$ differs for the Weyl fermions in the cones of different chirality. The resulting net imbalance in the global Hall current when summed over all Weyl nodes sets a finite axial current $\mathbf{j}^5 = \sum_n \mathbf{j}_n$ (or $\sum_+ \mathbf{j}_n - \sum_- \mathbf{j}_n$ as a difference of the currents with $+$ and $-$ chirality). On the other hand, the spin-momentum interlock in the Hamiltonian [Eq. (2)] establishes identity $\mathbf{j}_n = \eta_n q_e v_F \langle \mathbf{s} \rangle$ that determines a finite density of electron spin polarization $\langle \mathbf{s} \rangle = \zeta \mathbf{B}_5 \times \mathbf{E}$. The factor ζ can be evaluated under the relaxation-time approximation (t_r) in the quantum limit or a quasiclassical approach applied for the dense Landau levels [15]. In comparison, the contribution of the axial electric-field ($\mathbf{E}_5$) usually drops out of consideration due to its small strength [23]. Unlike the FM WSMs, where the induced net electron spin polarization (thus, the effective field) can exert directly a propulsive spin torque $\tau = (J\Omega/\hbar)\mathbf{m} \times \langle \mathbf{s} \rangle$ (Ω being the volume per magnetic ion) on the magnetic textures [15,16], the effect appears to be more complex for the Néel vector dynamics in the AFM counterparts as described in the following section.

Before proceeding further, let us discuss briefly the application of the model Hamiltonian [i.e., Eq. (2)] to the realistic AFM WSMs. In the FM WSMs (thus, with broken $\mathcal{T}$), one can conveniently presume the simplest structure of two nodes $n = 1, 2$ with opposite chirality $\eta_n = \pm 1$ under the $\mathcal{P}$ symmetry (i.e., a single pair of Weyl nodes) [15]. However, the AFM WSMs with a necessary weak magnetism via the DMI requires a more complex case with both $\mathcal{T}$ and $\mathcal{P}$ as well as the combined $\mathcal{TP}$ symmetry broken. As such, they must

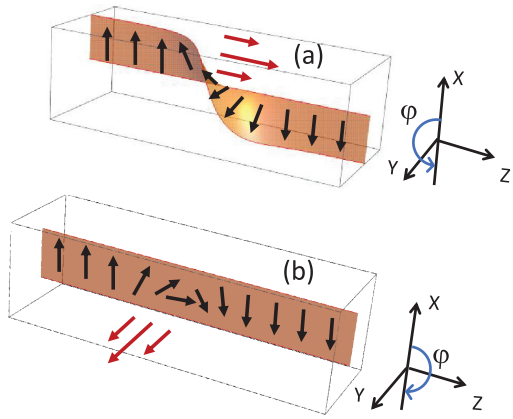

FIG. 1. Néel vector textures (black arrows) in the 180° (a) Bloch and (b) Néel DWs in an AFM WSM strip (on the $x-y$ and $x-z$ planes, respectively). The hard-axis $\widehat{\mathbf{e}}$ is oriented along the (a) $\widehat{\mathbf{z}}$ or (b) $\widehat{\mathbf{y}}$ direction. Without the DMI, the moving DWs generate the magnetization (of kinematic origin; red arrows) around the DW location with a fixed direction (a) along or (b) perpendicular to the direction of DW propagation (i.e., z). The reference angle $\varphi_0 = 0°$ is selected as shown for convenience.

contain, at least, two pairs of Weyl nodes of opposite chirality (i.e., $n = 1, 2$ and $n = 3, 4$). In the scarcity of AFM WSMs identified, thus, far reflecting the early stage of its research, a material interesting in this regard is $YbMnBi_2$ of space-group $p4/nmm$. It is a crystal in which magnetic ions (Mn) arrange a C-type AFM structure [24–26]. The AFM state displays four Dirac points under the combined $\mathcal{TP}$ symmetry, which preserves double degeneracy of the electronic bands. The necessary breaking of the remaining symmetry is introduced to the system when a portion of Bi atoms located on the plane farther away from Mn ions are substituted by defects (such as vacancies) or impurities. In the case of Bi vacancies, a recent calculation showed that the correspondent DMI creates an effective exchange field (via the canted spins of magnetic ions) capable of forming two pairs of topologically protected gapless band structure around the Fermi level [26]. Each of these nodes revealed a Weyl-type dispersion law at a modest exchange field described by the canonical Hamiltonian [Eq. (2)]. More generally, the desired AFM WSM structures can be realized in a solid solution $YbMn(Bi_{1-x}Z_x)_2$ with a minimally tangible concentration of vacancies or substitution by an atom Z isovalent to Bi [26]. Other examples are expected for this class of materials as the requirement is relatively straightforward to meet.

B. Exchange field of an axial current

The structure under consideration is an AFM WSM strip placed under an electric field whose direction coincides with that of the DW propagation along the z axis. More specifically, it is assumed that the interaction at the interface with the substrate gives rise to a broken C_4 symmetry perpendicular to the easy x axis. This structural anisotropy can establish a hard axis $\widehat{\mathbf{e}}$ and the conditions amenable for the emergence of a 180° DW as depicted in Fig. 1. The arrangement $\widehat{\mathbf{e}} \parallel \widehat{\mathbf{z}} = (0, 0, 1)$ supports a Bloch DW formation [Fig. 1(a)], whereas $\widehat{\mathbf{e}} \parallel \widehat{\mathbf{y}} = (0, 1, 0)$ shapes a Néel DW [Fig. 1(b)]. In the exchange approximation, such a disposition establishes the Néel vector $\mathbf{n}$ $(= \mathbf{L}/2M_s)$ located on the plane normal to the hard axis. It sets the unit vector $\mathbf{n}$ of the Bloch (Néel) DW to be on the $x-y$ $(z-x)$ plane, whose direction can be described in term of the azimuthal angle φ measured from the x axis, respectively; i.e., $\mathbf{n} = (\cos\varphi, \sin\varphi, 0)$ [or $(\cos\varphi, 0, \sin\varphi)$].

A basic solution for the 180° DW moving with a velocity v can benefit from a soliton representation against a reference angle φ_0 [14],

$$\varphi - \varphi_0 = \pm 2 \arctan(\exp \xi), \tag{3}$$

in terms of a self-similar variable with relativisticlike scaling,

$$\xi = \frac{z - vt}{\sqrt{1 - v^2}}. \tag{4}$$

Here, dimensionless length $z = z\omega_r/v_m$, time $t = t\omega_r$, and velocity $v = v/v_m < 1$ are used in place of those in physical units (i.e., z, t, v). In addition, ω_r and v_m denote the AFM resonant frequency and the magnon maximal velocity, respectively. Equation (3) satisfies the boundary conditions $\varphi - \varphi_0 = 0$ at $z \to -\infty$ and $\varphi - \varphi_0 = \pm\pi$ at $z \to \infty$ in which $\pm$ determines the chirality of the magnetic textures. The DW forms around $z = vt$ with an effective width $\pi\sqrt{1 - v^2}$ that shrinks as the velocity increases.

The application of a similar model [i.e., Eqs. (3) and (4)] to a FM DW texture directly describes the magnetization distribution $\mathbf{m}$ in terms of the azimuthal angle φ [i.e., $\mathbf{m}(\varphi)$]. By contrast, the AFM case generates a weak magnetization of two independent sources. The first one has the kinematic origin in the strong interlayer exchange interaction leading to a tilt in the sublattice magnetizations proportional to $\dot{\mathbf{n}} \times \mathbf{n}$ (where $\dot{\mathbf{n}} \equiv \frac{d}{dt}\mathbf{n}$). This produces a magnetization in the AFM DW,

$$\mathbf{m}_k = \frac{\omega_r}{\gamma H_{ex}} \frac{v}{2\sqrt{1 - v^2}\cosh \xi} \widehat{\mathbf{e}}, \tag{5}$$

where H_{ex} is the effective field of the AFM sublattice exchange interaction. The red arrows in Fig. 1 illustrate the $\mathbf{m}_k$ distribution along the AFM WSM strip. As the unidirectional $\mathbf{m}_k$ clearly does not exhibit any twist (i.e., torsion), its contribution to the axial magnetic field is expected to be negligible and, thus, ignored in following consideration.

Another source of the weak magnetization has a relativistic nature of the spin-orbit interaction. This can be sufficiently strong in the WSM to generate a magnetization $\mathbf{m}_d$ larger than $\mathbf{m}_k$ especially when the DW is not moving very fast. The particular dependence of $\mathbf{m}_d$ on the AFM-order parameter $\mathbf{n}$ stems from the magnetic symmetry that has a lot of variety [27]. To focus on the qualitative analysis of the DW dynamics in the AFM WSM, we restrict consideration to the instance of an easy-axis crystal with broken inversion symmetry (thus, enabling the DMI) as discussed earlier. The corresponding Néel vector can be described on a two-dimensional plane (e.g., $x-y$ or $x-z$ depending on the orientation of the hard-axis $\widehat{\mathbf{e}} \parallel \widehat{\mathbf{z}}$ or $\widehat{\mathbf{y}}$ shown in Fig. 1). Under such conditions, the contribution of the spin-orbit interaction to the magnetic energy can

be written in the form of Dzyaloshinskii's invariants [27]; i.e.,

$$D_{an} = w_D(n_x m_y - n_y m_x) - w_1(n_x m_y + n_y m_x) \quad \text{for } \widehat{\mathbf{e}} \parallel \widehat{\mathbf{z}}, \tag{6}$$

and

$$D_{an} = w_D(n_z m_x - n_x m_z) - w_1(n_z m_x + n_x m_z) \quad \text{for } \widehat{\mathbf{e}} \parallel \widehat{\mathbf{y}}. \tag{7}$$

Here, w_D denotes the strength of the DMI, and w_1 represents the relatively weak effect of the asymmetry induced by the structure anisotropy. Then, the term D_{an} leads to a weak magnetization, which can be expressed as [28]

$$\mathbf{m}_B = H_{ex}^{-1}[-(H_D + H_1)n_y, (H_D - H_1)n_x, 0] \tag{8}$$

or

$$\mathbf{m}_N = H_{ex}^{-1}[(H_D - H_1)n_z, 0, -(H_D + H_1)n_x], \tag{9}$$

in the Bloch and Néel DWs, respectively. The effective fields H_D and H_1 are defined as $w_D/2M_s$ and $w_1/2M_s$.

The following analysis shows that this weak magnetization results in efficient control of the DWs in both textures since it deflects the AFM magnetization $\mathbf{m}_{B[N]}$ from the hard axis [27,28]. Note that a strong spin-orbit interaction in the WSM induces H_D of sizable strength that can be sufficient to overcome thermal fluctuations randomizing the DW motion [14]; details of the thermal effects are outside the scope of the current investigation. Adopting the expression of the DW textures specifies the contribution of the DMI to the total magnetization as

$$\mathbf{m}_B = \left(-\frac{d_D + d_1}{\sqrt{1 + e^{2\xi}}}, \frac{(d_D - d_1)}{\sqrt{1 + e^{-2\xi}}}, 0\right), \tag{10}$$

$$\mathbf{m}_N = \left(\frac{d_D - d_1}{\sqrt{1 + e^{2\xi}}}, 0, -\frac{d_D + d_1}{\sqrt{1 + e^{-2\xi}}}\right), \tag{11}$$

where the normalized forms $d_D = H_D/H_{ex}$ and $d_1 = H_1/H_{ex}$ are used. Then, the axial magnetic field introduced by the DMI-related magnetization can be written in each Weyl cone as

$$\mathbf{B}_5^B = \eta \frac{\omega_r J}{q_e v_m \sqrt{1 - v^2}} \left(\frac{(d_D - d_1)e^{2\xi}}{(1 + e^{2\xi})^{3/2}}, -\frac{(d_D + d_1)e^{-2\xi}}{(1 + e^{-2\xi})^{3/2}}, 0\right), \tag{12}$$

$$\mathbf{B}_5^N = \eta \frac{\omega_r J}{q_e v_m \sqrt{1 - v^2}} \left(0, -\frac{(d_D - d_1)e^{2\xi}}{(1 + e^{2\xi})^{3/2}}, 0\right) \tag{13}$$

for the Bloch and Néel DWs, respectively. Vectors $\mathbf{B}_5^B$ and $\mathbf{B}_5^N$ lie on the plane perpendicular to the direction of DW propagation. In both cases, the axial fields are well localized around the instantaneous location $z \approx vt$ of the DW.

As discussed above, the external electric-field $\mathbf{E}$ combined with the intrinsic axial field $\mathbf{B}_5$ generates an axial current $\mathbf{j}^5$, which is associated with the electron-spin polarization density $\langle \mathbf{s} \rangle$ around the DW. In the subsequent analysis, our consideration is limited to the linear response regime where both the conventional electric current $\mathbf{j}_c$ and the induced spin current $\mathbf{j}^5$ are proportional to the strength of $\mathbf{E}$. This restriction presumes a small deviation of the nonequilibrium electron distribution function from its equilibrium state. Taking into account the relatively low density of states around the Weyl nodes, the suitable electric fields cannot be very strong. An appropriate range of the electric field is estimated later in the discussion. The appearance of the axial current $\mathbf{j}^5$ and net spin polarization $\langle \mathbf{s} \rangle$ subjects the AFM DW texture to a inhomogeneous nonstationary effective magnetic-field $\mathbf{H}_{el} = \gamma^{-1}\hbar^{-1}J\Omega\langle \mathbf{s} \rangle$, where γ is the gyromagnetic ratio. A straightforward calculation can lead to the final solutions for the effective field of the Weyl fermions,

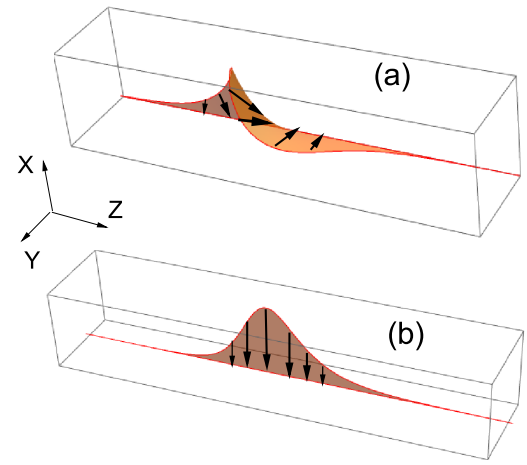

FIG. 2. Distribution of the effective exchange magnetic field $\mathbf{h}$ (black arrows) around the (a) Bloch and (b) Néel DWs in an AFM WSM strip. In both cases the chiral anomaly results in the spin polarization of Weyl fermions, which mediates the exchange fields.

$$\mathbf{h}^B = \frac{E}{E_0\sqrt{1 - v^2}} \left(-\frac{(1 + d_1/d_D)e^{\xi}}{(1 + e^{2\xi})^{3/2}}, -\frac{(1 - d_1/d_D)e^{2\xi}}{(1 + e^{2\xi})^{3/2}}, 0\right), \tag{14}$$

$$\mathbf{h}^N = \frac{E}{E_0\sqrt{1 - v^2}} \left(-\frac{(1 - d_1/d_D)e^{2\xi}}{(1 + e^{2\xi})^{3/2}}, 0, 0\right), \tag{15}$$

which are given with an electric-field $\mathbf{E} = (0, 0, E)$ for the Bloch and Néel DWs, respectively. The expressions adopt dimensionless units, i.e., $\mathbf{h} = \omega_r^{-1}\gamma\mathbf{H}_{el}$.

The nonzero components of $\mathbf{h}$ are shown in Fig. 2. In the case of a Bloch DW [Fig. 2(a)], the direction of the driving field varies along the DW texture, significantly reducing the net effect of the fieldlike angular force. By contrast, the contribution of the unidirectional effective field along the Néel DW texture $\mathbf{h}^N$ [Fig. 2(b)] appears cumulative and can, thus, be more efficient. Equations (14) and (15) also introduce a parameter E_0 in units of the electric field, whose magnitude depends on the strength of the axial magnetic field. Although a strong $\mathbf{B}_5$ can lead to the formation of well-defined cyclotron orbits within the relaxation time approximation, this condition is rather unlikely in realistic AFM WSMs with a weak magnetization. Thus, it is reasonable to adopt a quasiclassical approach when evaluating E_0 under the relaxation-time approximation [15],

$$E_0 = \frac{3\pi^2\hbar^4 v_F v_m}{q_e J^2 \Omega \mu t_r^2 d_D}, \tag{16}$$

where μ denotes the chemical potential. In the case of one pair of nodes, t_r depicts the relaxation time between the two cones of opposite chirality. For the structures, such as those under consideration with, at least, two pairs of Weyl nodes $n = 1, 2$ and $n = 3, 4$ (e.g., $+1$ for $n = 1, 2$ and -1 for $n = 3, 4$), the relaxation can involve multiple channels. Although the transitions within the nodes of the same chirality are more important to establish the conventional current, all criss-cross transfers between pairs of opposite chirality set the value of imbalance in the anomalous Hall current. In the case of four internode relaxation channels, (i) $K_1 \leftrightarrow K_3$, (ii) $K_2 \leftrightarrow K_4$, (iii) $K_1 \leftrightarrow K_4$, and (iv) $K_2 \leftrightarrow K_3$ reverse the chirality, whereas (v) $K_1 \leftrightarrow K_2$ and (vi) $K_3 \leftrightarrow K_4$ do not. The correspondent three characteristic times, i.e., t_a for transitions (i) and (ii); t_b for (iii) and (iv); and t_c for (v) and (vi), describe the rate of relaxation processes for fermions and their spin polarization. In the manner of the relaxation-time approximation, the net effect of these transition processes on the effective field $\mathbf{h}$ may be combined into a single empirical parameter t_r as in Eq. (16). The order of magnitude for t_r is estimated to be in several picoseconds.

The same quasiclassical approximation is applied to examine the upper range $E_{\max}$ of the electric field beyond which the validity of Ohm's law is in question. It can be estimated as a field at which the chiral imbalance in the electron population becomes comparable (or approximately equal) to that of equilibrium electrons in the conduction band; i.e., $E_{\max} \sim \mu/q_e v_F t_r$. Thus, the applicability of Eqs. (14) and (15) is restricted approximately by the inequality,

$$\frac{E}{E_0} < \frac{E_{\max}}{E_0} = \frac{J^2 \Omega \mu^2 t_r d_D}{3\pi^2 \hbar^4 v_F^2 v_m}. \tag{17}$$

A set of typical values $v_F = 4 \times 10^7$ cm/s, $\Omega = 2 \times 10^{-22}$ cm^3, $J = 0.6$, $\mu = 0.2$ eV, $t_r = 3$ ps, and $d_D = 4 \times 10^{-2}$ along with $v_m = 6.5 \times 10^7$ cm/s adopted from a well-known room-temperature AFM gives $E_0 \simeq 2$, $E_{\max}/E_0 \simeq 2$, or $E_{\max} \simeq 4$ kV/cm [29,30]. The suggested range of E indicates a relatively small strength of the effective field $\mathbf{h}$ when compared to the corresponding effective field in FM WSMs [15]. Nevertheless, a much faster response of the AFM textures on the external forces [11] can overcome the attenuation of electron spin polarization, revealing the potential advantage of AFM WSMs. A further discussion can be found later in Sec. III.

C. DW dynamics

The effective field [i.e., Eq. (14) or (15)] exerts a fieldlike angular force Φ to the AFM order parameter $\mathbf{n}$ via the angular acceleration $\ddot{\varphi}$ ($\equiv \frac{d^2}{dt^2}\varphi$) of its rotation, which is given as [31]

$$\Phi^{B[N]} = -\dot{h}_{z[y]} + \tfrac{1}{2} \sin 2\varphi \big(- h_{x[z]}^2 + h_{y[x]}^2 \big). \tag{18}$$

The term proportional to $\sin 2\varphi$ in Eq. (18) highlights the impact of the axial fields on the angular force in the WSM (thus, Weyl-type angular force) compared to that generated in a conventional system (e.g., via an electrical current in a heavy metal adjacent to a nontopological AFM [14]). Since $h_{z[y]} = 0$ according to Eqs. (14) and (15), this term becomes the only one responsible for the effective force in the Bloch and Néel DWs,

$$\Phi^B = \frac{1}{8(1-v^2)} \frac{E^2}{E_0^2} \frac{\left(1 + d_1^2/d_D^2\right) \tanh \xi - 2d_1}{(\cosh \xi)^3}, \tag{19}$$

$$\Phi^N = \frac{1}{(1-v^2)} \frac{E^2}{E_0^2} \frac{(1 - d_1/d_D)^2 e^{5\xi}}{(1 + e^{2\xi})^3}. \tag{20}$$

As mentioned above, the inequality $E \lesssim E_{\max}$ limits the applicability of both Eqs. (19) and (20).

The angular force $\Phi^{B[N]}$ applied to the order parameter rotating with a velocity $\dot{\varphi}$ establishes the rate of energy absorption by the moving DW as $W_{\text{in}}^{B[N]} = \int \Phi^{B[N]} \dot{\varphi} dz$ [14],

$$W_{\text{in}}^B = \frac{d_1}{6 d_D} \frac{E^2}{E_0^2} \frac{v}{1 - v^2}, \tag{21}$$

$$W_{\text{in}}^N = \frac{(1 - d_1/d_D)^2}{24} \frac{E^2}{E_0^2} \frac{v}{1 - v^2}. \tag{22}$$

As expected, the stationary AFM texture does not absorb the electromagnetic energy. Moreover, the electric field affects the Bloch DW through the weak structure anisotropy d_1 ($\ll d_D$) on the easy plane, which makes the driving of the Bloch DW less efficient than that of the Néel DW. The difference stems fundamentally from the alternating (vs uniform) direction of the DMI assisted effective magnetic field around the DW as it is qualitatively illustrated Fig. 2. In both cases, the energy absorption rate reveals a superlinear dependence on the DW velocity. This makes the usual relativistic (i.e., pertaining to the spin-orbit interaction) Gilbert-like dissipation mechanism with a dissipation function,

$$R_r = \lambda \dot{\mathbf{n}}^2 = \lambda \frac{v^2}{2\sqrt{1 - v^2}}, \tag{23}$$

insufficient to control the DW velocity. Thus, an additional mechanism of DW energy relaxation beyond the relativistic term in Eq. (23) must be considered.

A similar requirement to control the ultrafast dynamics in multilayer magnets necessitated to account for the exchange relaxation terms [32–34]. In a collinear AFM, they can be represented as an additive to the dissipation function [1,28],

$$R_e = \lambda_1 (\nabla [\mathbf{n} \times \dot{\mathbf{n}}])^2 + \lambda_2 \ddot{\mathbf{n}}^2, \tag{24}$$

where Onsager's relaxation parameters λ_1 and λ_2 survive even at zero spin-orbit interaction. Thus, the exchange relaxation can be of the same order of magnitude as the relativistic Gilbert terms λ [1,35]. The origin of the first term in Eq. (24) has a spin-diffusion nature that usually prevails over the second term at a low velocity $v \ll 1$ [28]. Incorporating R_e along with R_r to the net dissipation function modifies the dependence of the outgoing power on the DW velocity,

$$W_{\text{out}} = \lambda \frac{v^2}{\sqrt{1 - v^2}} + \frac{\lambda_1}{6} \frac{v^2}{(1 - v^2)^{3/2}} + \frac{\lambda_2}{4} \frac{v^4}{(1 - v^2)^{3/2}}. \tag{25}$$

It is remarkable that this dissipation function is equally applicable for Bloch and Néel DWs.

At low velocities, the dissipation $W_{\text{out}} \sim v^2$ is apparently unable to divert the power $W_{\text{in}} \sim v$ supplied to the Bloch or Néel DW. Accordingly, the excess power absorbed would

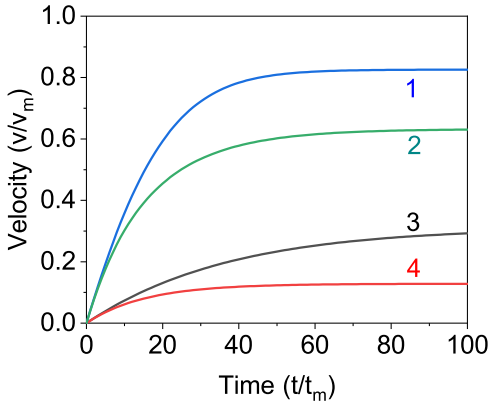

FIG. 3. AFM DW velocity as a function of time driven by the emergent angular force under an electric field $E = 0.5E_0$ and $d_1 = 0.1d_D$. Curves 1 and 2 are for the Néel DW, while curves 3 and 4 correspond to the Bloch DW. At $t = 0$, the DW is in a stationary state (i.e., $v = 0$). The damping parameters are assumed to be $\lambda = 0.01$ (curves 1 and 3) and $\lambda = 0.05$ (curves 2 and 4), respectively, while $\lambda_1 = 0.09$ and $\lambda_2 = 0.06$ are applied to all cases.

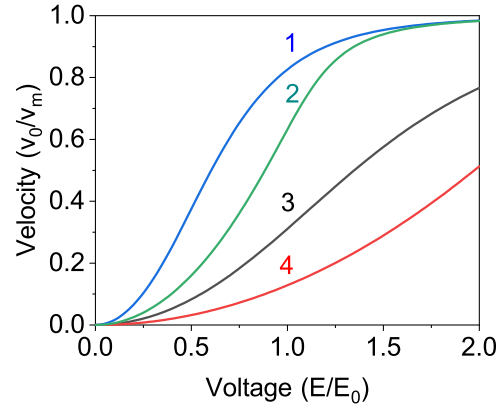

FIG. 4. Steady-state AFM DW velocity vs. applied electric field for Néel (curves 1 and 2) and Bloch DWs (curves 3 and 4) driven by the Weyl-type angular force under a condition $d_1 = 0.1d_D$. The range of the electric field is limited by $E_{\max}$ ($\approx 2E_0$). The damping parameters $\lambda_1 = 0.09$ and $\lambda_2 = 0.06$ are assumed for all cases, while $\lambda = 0.01$ (curves 1 and 3) and $\lambda = 0.05$ (curves 2 and 4) are used, respectively.

result in the acceleration of the DW motion whose energy increases with the velocity. To quantify this effect, it is necessary to evaluate the energy of the AFM texture $[\dot{\varphi}_t(\partial\mathcal{L}/\partial\dot{\varphi}_t) - \mathcal{L}]$ in terms of the Lagrangian $\mathcal{L} = \frac{1}{2}\dot{\varphi}_t^2 - \frac{1}{2}\dot{\varphi}_z^2 - \frac{1}{8}\sin^2 2\varphi$ of the DW, where $\dot{\varphi}_i \equiv \frac{\partial}{\partial i}\varphi$ $(i = x, t)$ [14]. A straightforward calculation reveals the implicit DW energy dependence on the velocity as $E_{DW}(v) = \frac{1}{2}(1 - v^2)^{-1/2}$. Thus, the temporal evolution of the DW velocity obeys the equation,

$$\frac{dv(t)}{dt}\frac{v}{2(1-v^2)^{3/2}} = W_{\text{in}}^{B[N]} - W_{\text{out}}. \tag{26}$$

In the nontrivial case of $v \neq 0$, the above expression reduces to

$$\frac{dv_{B[N]}}{dt} = \frac{E_{B[N]}^2}{E_0^2}\sqrt{1-v^2} - \lambda v(1-v^2) - \frac{\lambda_1}{6}v - \frac{\lambda_2}{4}v^3, \tag{27}$$

where

$$E_B^2 = \frac{d_1}{6d_D}E^2, \tag{28}$$

and

$$E_N^2 = \frac{(1 - d_1/d_D)^2}{24}E^2. \tag{29}$$

III. RESULTS AND DISCUSSION

Numerical solutions of Eq. (27) with parameter values adopted from the FM WSM [15] and typical AFM crystals [6,26,28,29] (as specified in Sec. II B) show that the DW starting its acceleration with $v = 0$ reaches a higher velocity faster with the smaller dissipation terms even at the same electric-field E (Fig. 3). This behavior is akin to the transient electron transport well known in semiconductors. Evidently, a larger excess power as a result of a smaller loss in the initial stage translates into a larger effective force that can push the DW to a higher speed more rapidly. Once the DW velocity becomes sizable (vs v_m), the driving force [i.e., the first term on the right side of Eq. (27)] starts to diminish whereas the drag grows quickly (in particular, the R_e terms) at the same time, bringing further acceleration to a stand still (at a higher steady-state value of v_s). One interesting observation, in contrast to the FM WSMs [15], is that the Néel DW tends to gain speed faster than the Bloch counterpart. This is consistent with the discussion made earlier in Sec. II C on the varying direction of the effective field $\mathbf{h}^B$ generated by the axial current in the Bloch DW [see also Fig. 2(a)]. The resulting compensation at the leading and trailing edges of the DW significantly weakens the induced net angular force. In comparison, the accumulative contribution of the unidirectional field $\mathbf{h}^N$ amplifies the effect of the DMI on the angular force in the Néel DW [Fig. 2(b)].

The steady-state velocity v_s for a given electric field can be obtained from the condition in which the balance between the incoming and outgoing power is achieved (i.e., at $W_{out} = W_{in}$). Figure 4 provides the resulting DW velocity vsapplied electric field in AFM WSMs. At a low E, the steady-state velocity v_s grows proportional to E^2 due to the quadratic dependence of the angular forces on E for both DW modes [Eqs. (19) and (20)] (see also Ref. [1]). Similar to the discussion in Fig. 3, the leading driving term decreases with the increasing velocity (thus, the electric-field E). This saturation behavior is seen most prominently in the case with the highest velocity (i.e., curve 1) as the effect becomes significant only when the DW velocity approaches to the ultimate value $v \to 1$ (i.e., the magnon maximal velocity v_m). Curve 2 follows suit at higher electric fields, asymptotically converging at v_m. By comparison, curves 3 and 4 (for the Bloch DW) remain virtually unaffected by the deviation from the E^2 dependence since the velocity remains low within the field range considered (i.e., $E \lesssim E_{\max}$).

The observed quadratic dependence also leads to an interesting phenomenon of velocity invariance when the sign (i.e., polarity) of the applied electric field changes. This is in stark contrast to the FM counterparts where the DW velocity reverses accompanying that of the induced spin torque (thus, the applied electric field) [15]. In the absence of an alternating

field [i.e., nonzero $\dot{h}_{z[y]}$ in Eq. (18)], the direction of the DW movement in an AFM WSM is actually determined by the mutual orientation of the Néel vectors in both domains. The particular Bloch DW texture shown in Fig. 1(a) corresponds to the Néel vector orientation of $\varphi = 0^\circ$ in the left-side domain and $\varphi = 180^\circ$ in the right side. In such a case, the positive change in φ (i.e., $0^\circ \rightarrow 180^\circ$) prescribes the DW transfer toward the right-side domain, i.e., $v > 0$. Likewise, the Néel DW illustrated in Fig. 1(b) is also with a positive DW velocity where the Néel vector orientations in the left- and right-side domain edges are set to $\varphi = 0^\circ$ and $\varphi = 180^\circ$, respectively. On the other hand, the DW moves in the opposite direction (i.e., $v < 0$) when the chirality of the DW is reversed.

The analysis provided above for electrical control of the DWs in the AFM WSMs clearly illustrates the unique features stemming from the weak ferromagnetism of the AFM DWs. Namely, the most important consequence is that the DMI mediates an axial current in an electric field. This develops a force available to push both Bloch and Néel DWs along the AFM WSM strip. The efficiency of the torque induced in FM vs the angular force in AFM WSM thin films can be compared by following the estimation provided in Ref. [15]. Using the same set of parameters applied to evaluate $E_{\max}$, the authors of Ref. [15] found that an electric-field $E = 1$ kV/cm can establish the DW velocity $v_s \sim 2.8 \times 10^5$ cm/s in FM WSMs. On the other hand, our calculation as summarized in Fig. 4 indicates a velocity of $\sim 2.6 \times 10^7$ cm/s for the Néel DW (curve 1) that is almost two orders of magnitude higher. Note also that the field strength $E \sim 1$ kV/cm corresponds to a relatively modest electrical current density of $\sim 1.5 \times 10^7$ A/cm^2. At this level of the driving current density, the DW velocity in the conventional AFMs is expected to reach a value that is an order-of-magnitude smaller (e.g., $\sim 2.4 \times 10^6$ cm/s [12]).

Our quantitative estimation, as described, is based on a set of material parameter values, some of which are derived from FM counterparts rather than the desired AFM WSMs. Recent *ab initio* calculations of $\beta - Fe_2PO_5$ [36], Bi_2MnSe_4 [37], and $LiTi_2O_4$ with D_4-crystalline point-group symmetry [38] have added potential instances of AFM WSMs to the list of candidates including Mn_3X (X=Ge, Sn), $X_2Ir_2O_7$ (X=Nd, Y, Eu), and $YbMn(Bi_{1-x}Z_x)_2$ [19,26]. However, the lack of an available set of parameters remains a key challenge to a limited number of AFM WSMs identified, thus far. Although the actual AFM WSM structures may possess the properties different from those assumed, no physical obstacle is expected in applying the approach developed in this paper to more realistic cases.

IV. SUMMARY

We examine the nontrivial effect of an external electric field on the Bloch and Néel DWs in AFM WSMs with broken inversion symmetry. A formal analogy with the massless Dirac Hamiltonian in the Weyl cones of opposite chirality enables the description of the electron exchange interaction with a magnetic moment in terms of the axial vector potential. As the torsion in this vector potential (thus, in the magnetization distribution of the Néel vector textures) expresses itself as an axial magnetic field, the unidirectional kinematic magnetization of a moving AFM DW cannot produce the effective axial field. By contrast, our investigation illustrates that the introduction of a DMI can provide the necessary twist in the magnetization distribution. The resulting nonzero axial magnetic field, when combined with an external electric field, induces an imbalance in the Hall currents of the Weyl cones of opposite chirality (i.e., the axial anomaly), leading to a net electron spin polarization via the strong spin-orbit coupling. Finally, the spin-polarized Weyl fermions create an effective exchange field that affects the Néel vector texture in the form of a fieldlike angular force capable of moving the DW. The effect of multiple Weyl-node pairs is treated empirically in a relaxation-time approximation.

The DW response to this emergent force is analyzed in an AFM WSM strip by considering the balance (or imbalance) between the absorbed and dissipated powers. The results reveal that this Weyl-type mechanism is significantly less effective in driving the Bloch DW than the Néel counterpart. The difference appears to be due to the more symmetrical nature of the Bloch DW texture, leading to the angular forces applied at the leading and trailing edges largely compensating each other. As such, the net contribution derives only from a relatively weak magnetic anisotropy on the easy plane. By contrast, such an additional asymmetry is not needed for the Néel DW, making its electrical control quite efficient compared to other magnetoelectric mechanisms. Indeed, our numerical evaluation illustrates that the Néel DW in AFM WSMs can achieve a significant speedup in the obtained DW velocity vs electric-field characteristics over the counterparts in the FM WSMs. When compared to nontopological magnets, the Weyl-type angular force appears to be much more energy efficient in driving the magnetic textures. Our results also show that the particularities of the axial magnetic field dictate the direction of the AFM DW motion to be invariant to the polarity of the applied electric field. Although this feature could impose a limitation in the practical applications despite the high-energy efficiency, the unique dependence on the chirality of the magnetic textures presents interesting physics and may prove to be useful in multidomain structures.

ACKNOWLEDGMENTS

This work was supported, in part, by the U.S. Army Research Office (Grant No. W911NF-20-2-0166).

[1] E. V. Gomonay and V. M. Loktev, Spintronics of antiferromagnetic systems, Low Temp. Phys. **40**, 17 (2014).

[2] R. Cheng, M. W. Daniels, J.-G. Zhu, and D. Xiao, Ultrafast switching of antiferromagnets via spin-transfer torque, Phys. Rev. B **91**, 064423 (2015).

[3] T. Jungwirth, X. Marti, P. Wadley, and J. Wunderlich, Antiferromagnetic spintronics, Nat. Nanotechnol. **11**, 231 (2016).

[4] O. Gomonay, T. Jungwirth, and J. Sinova, Concepts of antiferromagnetic spintronics, Phys. Status Solidi RRL **11**, 1700022 (2017).

[5] T. Jungwirth, J. Sinova, A. Manchon, X. Marti, J. Wunderlich, and C. Felser, The multiple directions of antiferromagnetic spintronics, Nat. Phys. **14**, 200 (2018).

[6] V. Baltz, A. Manchon, M. Tsoi, T. Moriyama, T. Ono, and Y. Tserkovnyak, Antiferromagnetic spintronics, Rev. Mod. Phys. **90**, 015005 (2018).

[7] B. A. Ivanov, Ultrafast spin dynamics and spintronics for ferrimagnets close to the spin compensation point (Review), Low Temp. Phys. **45**, 935 (2019).

[8] Y. G. Semenov and K. W. Kim, Spin-transfer and fieldlike torques in antiferromagnets, Phys. Rev. B **104**, 174402 (2021).

[9] X. Z. Chen, R. Zarzuela, J. Zhang, C. Song, X. F. Zhou, G. Y. Shi, F. Li, H. A. Zhou, W. J. Jiang, F. Pan, and Y. Tserkovnyak, Antidamping-Torque-Induced Switching in Biaxial Antiferromagnetic Insulators, Phys. Rev. Lett. **120**, 207204 (2018).

[10] A. Manchon, J. Železný, I. M. Miron, T. Jungwirth, J. Sinova, A. Thiaville, K. Garello, and P. Gambardella, Current-induced spin-orbit torques in ferromagnetic and antiferromagnetic systems, Rev. Mod. Phys. **91**, 035004 (2019).

[11] Y. G. Semenov, X.-L. Li, and K. W. Kim, Currentless reversal of Néel vector in antiferromagnets, Phys. Rev. B **95**, 014434 (2017); Y. G. Semenov and K. W. Kim, Spin Pumping Torque in Antiferromagnets, Appl. Phys. Lett. **110**, 192405 (2017).

[12] O. Gomonay, T. Jungwirth, and J. Sinova, High Antiferromagnetic Domain Wall Velocity Induced by Néel Spin-Orbit Torques, Phys. Rev. Lett. **117**, 017202 (2016).

[13] T. Shiino, S.-H. Oh, P. M. Haney, S.-W. Lee, G. Go, B.-G. Park, and K.-J. Lee, Antiferromagnetic Domain Wall Motion Driven by Spin-Orbit Torques, Phys. Rev. Lett. **117**, 087203 (2016).

[14] Y. G. Semenov, X. Xu, and K. W. Kim, Controllable Dispersion of Domain-Wall Movement in Antiferromagnetic Thin Films at Finite Temperatures, Phys. Rev. Appl. **11**, 064051 (2019).

[15] D. Kurebayashi and K. Nomura, Theory for spin torque in Weyl semimetal with magnetic texture, Sci. Rep. **9**, 5365 (2019).

[16] D. Kurebayashi, Y. Araki, and K. Nomura, Microscopic theory of electrically induced spin torques in magnetic Weyl semimetals, J. Phys. Soc. Jpn. **90**, 084702 (2021).

[17] J. D. Hannukainen, A. Cortijo, J. H. Bardarson, and Y. Ferreiros, Electric manipulation of domain walls in magnetic Weyl semimetals via the axial anomaly, SciPost Phys. **10**, 102 (2021).

[18] N. P. Armitage, E. J. Mele, and A. Vishwanath, Weyl and Dirac semimetals in three-dimensional solids, Rev. Mod. Phys. **90**, 015001 (2018).

[19] L. Šmejkal, L. Šmejkal, and J. Sinova, Route towards Dirac and Weyl antiferromagnetic spintronics, Phys. Status Solidi RRL **11**, 1700044 (2017).

[20] Y. Tserkovnyak, Magnetic dynamics with Weyl fermions, Phys. Rev. B **103**, 064409 (2021).

[21] J. Yu, B. Yan, and C.-X. Liu, Model Hamiltonian and time reversal breaking topological phases of antiferromagnetic half-Heusler materials, Phys. Rev. B **95**, 235158 (2017).

[22] A. Sekine and K. Nomura, Axion electrodynamics in topological materials, J. Appl. Phys. **129**, 141101 (2021).

[23] Y. Araki and K. Nomura, Charge Pumping Induced by Magnetic Texture Dynamics in Weyl Semimetals, Phys. Rev. Appl. **10**, 014007 (2018).

[24] S. Borisenko, D. Evtushinsky, Q. Gibson, A. Yaresko, K. Koepernik, T. Kim, M. Ali, J. van den Brink, M. Hoesch, A. Fedorov, E. Haubold, Y. Kushnirenko, I. Soldatov, R. Schafer, and R. J. Cava, Time-reversal symmetry breaking type-II Weyl state in $YbMnBi_2$, Nat. Commun. **10**, 3424 (2019).

[25] Z. Zhu, D. Yan, X. A. Nie, H. K. Xu, X. Yang, D. D. Guan, S. Wang, Y. Y. Li, C. Liu, J. W. Liu, H. X. Luo, H. Zheng, and J. F. Jia, Scanning tunneling microscopic investigation on morphology of magnetic Weyl semimetal $YbMnBi_2$, Chin. Phys. B **28**, 077302 (2019).

[26] X.-S. Ni, C.-Q. Chen, D.-X. Yao, and Y. Hou, Origin of the type-II Weyl state in topological antiferromagnetic $YbMnBi_2$, Phys. Rev. B **105**, 134406 (2022).

[27] E. A. Turov, *Symmetry and Physical Properties of Antiferromagnetics* (Cambridge, Cambridge, UK, 2010), Chap. 8.

[28] B. A. Ivanov and D. D. Sheka, Soliton (vortex) thermodynamics of a quasi-2D easy-plane antiferromagnet, JETP **80**, 907 (1995).

[29] K. Lee, D.-K. Lee, D. Yang, R. Mishra, D.-J. Kim, S. Liu, Q. Xiong, S. K. Kim, K.-J. Lee, and H. Yang, Superluminal-like magnon propagation in antiferromagnetic NiO at nanoscale distances, Nat. Nanotechnol. **16**, 1337 (2021).

[30] Note that a lower magnon velocity is often assigned to the low-temperature AFMs with a weaker exchange field H_{ex}. This may rescale the numerical value of E_0 [Eq. (16)], which is outside the scope of the current investigation.

[31] Y. G. Semenov, X. Xu, and K. W. Kim, Thermal fluctuations in antiferromagnetic nanostructures, J. Magn. Magn. Mater. **489**, 165457 (2019).

[32] J. H. Mentink, J. Hellsvik, D. V. Afanasiev, B. A. Ivanov, A. Kirilyuk, A. V. Kimel, O. Eriksson, M. I. Katsnelson, and T. Rasing, Ultrafast Spin Dynamics in Multisublattice Magnets, Phys. Rev. Lett. **108**, 057202 (2012).

[33] V. G. Bar'yakhtar, V. I. Butrim, and B. A. Ivanov, Exchange relaxation as the mechanism of ultrafast spin reorientation in two-sublattice ferrimagnets, JETP Lett. **98**, 289 (2013).

[34] I. A. Yastremsky, J. Fassbender, B. A. Ivanov, and D. Makarov, Enhanced Longitudinal Relaxation of Magnetic Solitons in Ultrathin Films, Phys. Rev. Appl. **17**, L061002 (2022).

[35] J. Linder, Controllable spin-transfer torque on an antiferromagnet in a dual spin-valve, Phys. Rev. B **84**, 094404 (2011).

[36] T. He, X. Zhang, W. Meng, L. Jin, X. Dai, and G. Liu, Topological nodal lines and nodal points in the antiferromagnetic material β-Fe_2PO_5, J. Mater. Chem. C **7**, 12657 (2019).

[37] S. Chowdhury, K. F. Garrity, and F. Tavazza, Prediction of Weyl semimetal and antiferromagnetic topological insulator phases in Bi_2MnSe_4, npj Comput Mater **5**, 33 (2019).

[38] T. He, X. Zhang, Y. Liu, X. Dai, L. Wang, and G. Liu, Potential antiferromagnetic Weyl nodal line state in $LiTi_2O_4$ material, Phys. Rev. B **104**, 045143 (2021).